Tonegawa and Fukao
Earth, Planets and Space (2022) 74:159
https://doi.org/10.1186/s40623-022-01727-x

Earth, Planets and Space

EXPRESS LETTER

Open Access

Wave propagation of meteotsunamis and generation of free tsunamis in the sloping area of the Japan Trench for the 2022 Hunga–Tonga volcanic eruption

Takashi Tonegawa* and Yoshio Fukao

Abstract

Meteotsunamis (forced waves) triggered by atmospheric disturbances of Lamb waves due to the 2022 Hunga–Tonga volcanic eruption have been observed in coastal areas surrounding the Pacific Ocean. However, the spatiotemporal evolution of the wavefield of meteotsunamis and meteotsunami-induced free waves remains elusive. Here, we show the detailed spatial distribution of the propagation velocities and directions of these waves in the bathymetric slope area between the Japan Trench and nearshore, using a dense array of 150 absolute pressure gauges deployed at water depths of 100–8000 m. Records show that free wave components (i.e., tsunamis) were generated when the forced wave was propagating over the slope area. Amplitudes of the generated free waves are large in the southern half of the slope area, where the equi-arrival time contour lines are densely paralleled. Such amplifications occur due to the relationship between the incoming direction of Lamb waves and the gradient of the bathymetric slope. This indicates that, if meteotsunamis excited by Lamb waves due to future volcanic eruptions come from different directions to this region, a different spatial pattern of free wave amplification on a regional scale is obtained in the bathymetric slope areas.

Keywords: 2022 Hunga–Tonga volcanic eruption, Meteotsunami, Lamb wave, Free wave

*Correspondence: tonegawa@jamstec.go.jp

Japan Agency for Marine-Earth Science and Technology (JAMSTEC), 3173-25, Showa-Machi, Kanazawa-Ku, Yokohama 236-0001, Japan

Graphical Abstract

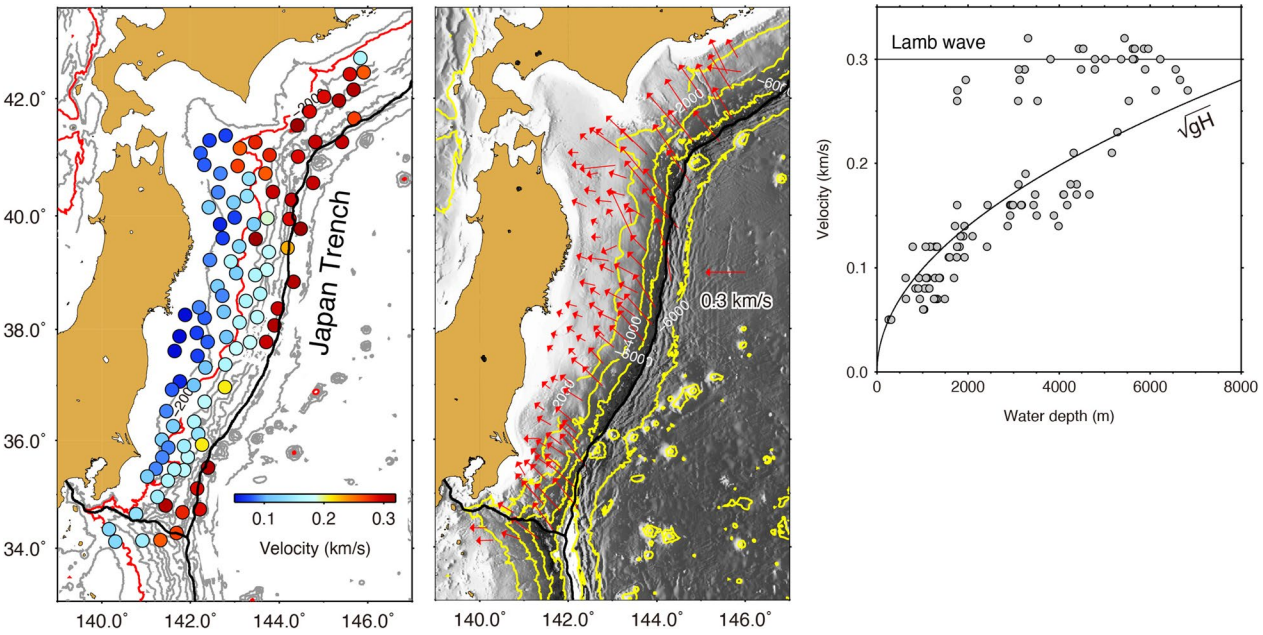

Main text

Introduction

A large eruption occurred at the Tonga–Hunga Ha'apai volcano in Tonga on 15 January 2022 (UT). Lamb waves (Lamb 1932), which were triggered by the eruption, were recognized worldwide as the first arrival of atmospheric disturbances, and sea level changes were also observed at the timing of the Lamb wave propagation in the Pacific Ocean (Kubota et al. 2022). A previous study (Harkrider and Press 1967), calculating existing gravity modes in the atmosphere–ocean coupled system, reproduced waveforms of the Lamb waves and the Lamb-wave induced sea level change for the Krakatoa volcano case. They also pointed out that subsequently arriving waves can be observed in the sea level changes and air pressures. The subsequently arriving waves from the Tonga eruption were observed with a time delay of > 2 h from the Lamb wave arrivals, and are caused by the contaminations of waves excited by different mechanisms: (1) free waves associated with crustal deformation of the volcanic eruption and (2) tsunami mode coupled with gravity modes in the atmosphere (Kubota et al. 2022). Here, surface gravity waves propagating in the ocean that are not driven by atmospheric disturbances, but by the restoring gravity force, are free waves (or free tsunamis) (e.g., Garrett 1970; Vilibić 2008).

Meteotsunamis are atmospherically induced tsunami-like waves (Defant 1961; Monserrat et al. 2006), and the sea level change excited by the Lamb waves from the volcanic eruption can be categorized as a meteotsunami. Here, the sea level changes forced by Lamb waves due to the Tonga volcanic eruption are meteotsunamis (or forced waves) (e.g., Garrett 1970; Vilibić 2008). The characteristics of meteotsunamis excited by a regional- or local-scale phenomenon in the atmosphere have been investigated via sea (and tide) level measurements (Monserrat et al. 2006), and these in situ measurements have been compared to results obtained through numerical simulations (Vilibić 2008; Chen and Niu 2018). For the 2022 Tonga eruption, comparisons between synthetic and observed waveforms have been performed at global and regional scales (Kubota et al. 2022; Tanioka et al. 2022). However, since meteotsunamis excited by Lamb waves are seldom observed, their characteristics and the detailed wavefields, including the spatial variation of the propagation velocity and direction, remain elusive. To investigate this phenomenon, spatially dense geophysical observations in the ocean are useful.

The Seafloor Observation Network for Earthquakes and Tsunamis (S-net) (Aoi et al. 2020), a dense offshore observation network, has recently been constructed off the eastern coast of Japan (Fig. 1a). The

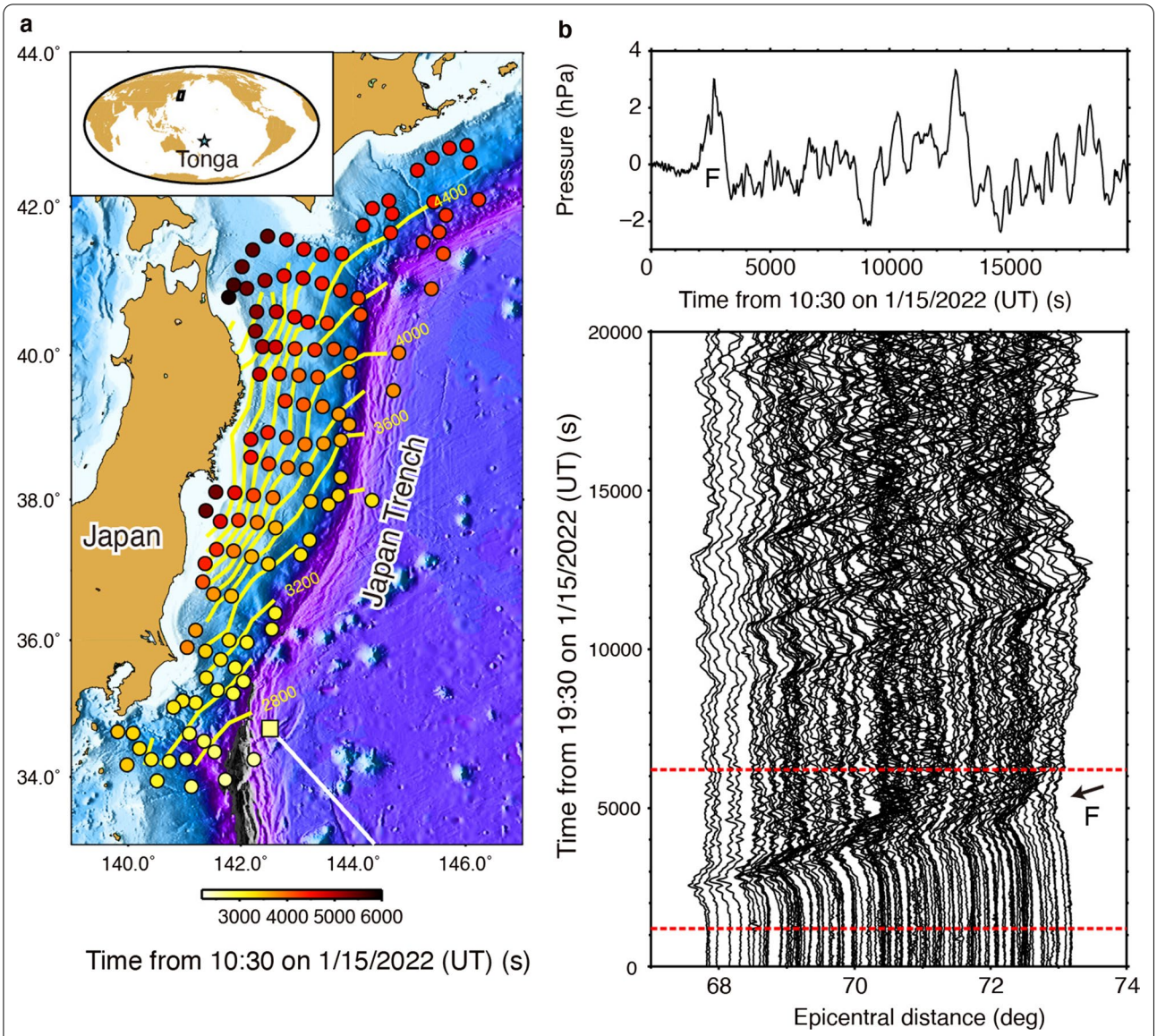

Fig. 1 Geometry of the observation for the Tonga volcanic eruption and the waveforms of the absolute pressure gauges (APGs). **a** Arrival times of the peaks of the meteotsunamis (label F in **b**) at each station of S-net. Yellow lines show the contour lines of the arrival times. Inset represents the location of the Hunga–Tonga volcano. Square indicates the island station N.S6N19. The white line connects the N.S6N19 with the Tonga volcano along the great circle. **b** APG waveform after removing the long-period components for (top) a station N.S6N19 and (bottom) all of the used stations. The red dashed lines represent the time window of 5000 s for searching the arrival times of the first peaks

S-net stations contain absolute pressure gauges (APGs). Analyses of these APG records have made it possible to detect meteotsunamis of atmospheric pressure origin (Kubota et al. 2021) and volcanic eruption origin (Kubo et al. 2022; Yamada et al. 2022). Using the APG records observed in the 2022 Tonga event, we show the wavefields for the meteotsunami and the meteotsunami-induced free waves across the bathymetric slope areas from the trench to the nearshore in this study. Our results contribute to the understanding of how free waves are generated during the meteotsunami propagation and why the nearshore sea level changes are different along the coast on a regional scale.

Data and methods

Absolute pressure gauge records

The S-net contains 150 stations deployed at a water depth of 100–8000 m with the station spacing for the north–south and east–west station configurations at 50 km and 30 km, respectively. Two pressure gauges (HP1WP and HP2WP) are equipped at each station. Because the

number of the broken APGs for HP1WP is large (Wang and Satake 2021), we use APG records for HP2WP in this study.

Long-period components, such as ocean tides, are contained in the continuous records of APGs deployed on the seafloor. To investigate the waveforms of meteotsunamis, we remove the long-period components from the records by fitting the fifth-order polynomial functions (Additional file 1: Fig. S1). The time window for the fitting is the 3 h between 10:00 and 13:00 (UT) on 1/15/2022. An example for fitting of the waveform observed at station N.S6N19 is shown in Additional file 1: Fig. S1a, and the trace subtracting the fitted function is displayed in Fig. 1b and Additional file 1: Fig. S1b. In addition to broken APGs, we did not use traces unstable fittings, and the total number of the used traces was 123. We then use the processed traces in the subsequent sections; they are aligned as a function of epicentral distance (Fig. 1c). The label of "F" indicates the first arrivals with a positive polarity and a duration of ~ 2000s, which correspond to meteotsunamis induced by the Lamb waves or generated free waves: as discussed later, the maximum amplitudes of the first arrivals in the seafloor pressure at the bathymetric slope area are delayed from those of the Lamb waves, hence the maximum amplitudes in the seafloor pressure correspond to either meteotsunamis or generated free waves. Here, the amplitudes in the seafloor pressure mainly result from both the air pressure changes of the Lamb waves above the sea surface and induced sea level changes (Saito et al. 2021; Kubota et al. 2022; Tanioka et al. 2022). Subsequent waves corresponding to atmospheric gravity modes coupled with the ocean can also be observed after the first arrivals at a time window of 7000–17,000 s (Fig. 1c); however, we focus on the wave propagation of the first arrivals in this study.

Measurement of propagation velocity and direction

Figure 1A shows the arrival times for the peaks in the first arrivals, where the peak is defined as the maximum amplitude in the time window of 5000 s indicated by red dashed lines in Fig. 1b. To measure the apparent propagation velocity and direction, we set 102 triangular subarrays (triads) that comprise three S-net stations (Additional file 1: Fig. S2a) (Okuwaki et al. 2021). The center location of a triad is estimated by averaging the locations of the three stations. The reference arrival time at the center (T_r in Additional file 1: Fig. S3) is estimated at each triad by averaging arrival times of the three stations ($(T_1+T_2+T_3)/3$, where T_i ($i=1, 2, 3$) is the arrival times of the three stations), and the differential times from the averaged value at the center are obtained:

$$\Delta t_i = T_i - T_r (i = 1, 2, 3) \quad (1)$$

We assume that a plane wave enters the triad with a pair of propagation velocity and direction. Because we can calculate the distances (d_i, $i=1, 2, 3$) between the three stations and wavefront with a propagation direction (θ), which is measured clockwise from the north, the theoretical differential times (τ_i, $i=1, 2, 3$) can be calculated with a propagation velocity (c) and these distances (d_i) (Additional file 1: Fig. S3):

$$\tau_i = d_i/c (i = 1, 2, 3) \quad (2)$$

Using a grid search, we estimate a suitable pair of those values (c and θ) that minimize the difference between the observed and theoretical differential times at each triad, S, where S is given by the following equation:

$$S(c, \theta) = \sum_{i=1}^{3} |\Delta t_i - \tau_i| \quad (3)$$

The search range and increment for propagation velocity are 0.05–0.40 km/s and 0.01 km/s, respectively, and those for direction are 0°–360° and 1°, as measured clockwise from the north. An example of Eq. (3) is shown in Additional file 1: Fig. S4. The error range, which is defined by twice the minimum value (Umino et al. 2002), is shown by red line; however, the error is quite small, indicating a robust estimation on the propagation velocity and direction. Moreover, we set 282 triads with the highest densities in the S-net, and calculate the propagation direction and velocity for a comparison with those for the 102 triads. The averaged one-side lengths of the 102 and 282 triads and their standard deviations are 67.0 ± 16.7 km and 50.2 ± 31.8 km, respectively. The resulting propagation velocity and direction for the 102 triads are shown in Fig. 2a, Additional file 1: Fig. S2b and Table S1, while those for the 282 triads are shown in Additional file 1: Fig. S5.

Measurement of propagation velocity and direction of Lamb wave

To investigate the characteristics of waveforms, e.g., peak duration and delay, between Lamb waves in the air pressure and the meteotsunamis in the seafloor pressure, we estimate apparent velocities of Lamb waves, and compare a barometer record with APG records with time shifts using the estimated velocity. In the Japanese Islands, barometers have been deployed at volcanoes by the volcano observation network (V-net) (https://doi.org/10.17598/nied.0006) (Additional file 1: Fig. S6a), and the Lamb wave associated with the 2022 Tonga volcanic eruption was observed via these barometers (Additional file 1: Fig. S6b, c). As shown in Additional file 1: Fig. S6a, we set triads using a part of the barometers to estimate the apparent propagation velocity of the Lamb wave. The

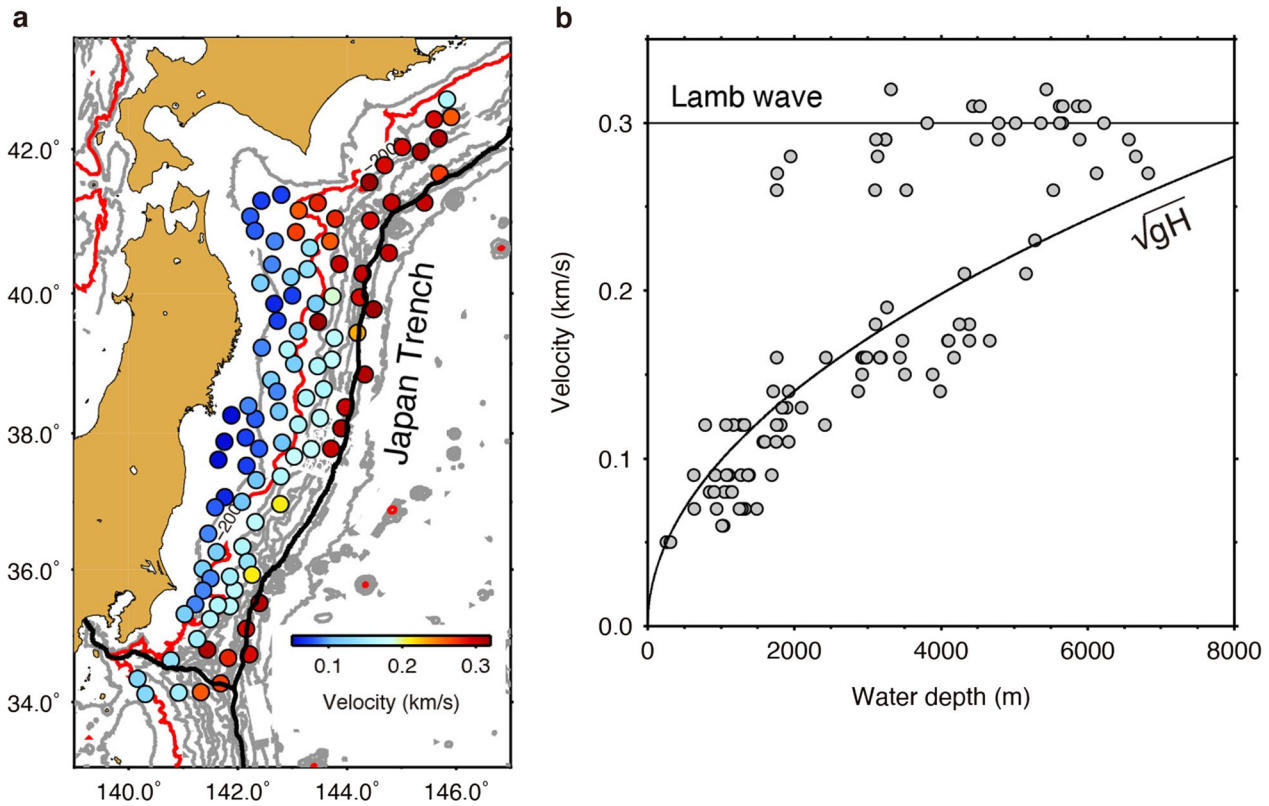

Fig. 2 Propagation velocities of meteotsunamis and free waves. **a** Propagation velocities at the centers of the triads. **b** Plot for propagation velocity of the first arrival versus water depth *H*. Curved line indicates the tsunami wave velocity $\sqrt{gH}$, where *g* is the gravitational acceleration. The horizontal line represents a typical Lamb wave velocity of 0.3 km/s

method for estimating propagation velocity and direction is the same as that used for the ocean bottom pressure, but we used the peak amplitude of the Lamb waves for measuring the arrival times.

The estimated propagation velocity and direction of the Lamb waves are shown in Additional file 1: Fig. S6a. In the region south of 40° N, the propagation velocity and direction at the triads are around 0.29 km/s (up to 0.3 km/s) and 315°–319°, respectively. We compare the waveforms of a barometer and APGs, using the propagation velocity of 0.29 km/s (Fig. 3b). The waveforms of APGs were time-shifted using the propagation velocity of 0.29 km/s and the epicentral distance difference between the barometer station of N.MKAV (Miyakejima Island) and each APG. The island is located in the southern part of the Japanese Islands, and it is considered that the barogram of the Lamb wave coming from the southeast direction is not significantly affected by inland topographic factors. At the northern triads, estimated propagation velocities and directions are slightly different from those at the southern triads. Because peak shapes of the Lamb waves at northern stations are slightly different from those at the southern stations, particularly at epicentral distances greater than 74° (Additional file 1: Fig. S6), those waveforms may be affected by the inland topography, and result in the different estimations.

Results

Propagation velocity and direction

Figure 1A shows that the obtained contour intervals of the arrival times are not uniform, indicating that the apparent propagation velocities of the peaks change spatially between the Japan Trench and nearshore. While the measured propagation velocity for the peaks is close to 0.3 km/s seawards near the Japan Trench, which is comparable to the propagation velocity of 0.31 km/s for the Lamb wave estimated using background noise records (Nishida et al. 2014), it decelerates landwards and becomes 0.05 km/s nearshore (Fig. 2a).

Previous numerical simulations show that the propagation velocities of the meteotsunamis changes to those of the free waves (tsunami) over the bathymetric slope (Vilibić 2008; Sekizawa and Kohyama 2022). Therefore, we investigate how the obtained apparent wave velocities approaches to the propagation velocity of the long wave: $\sqrt{gH}$, where g is the gravitational acceleration and H is

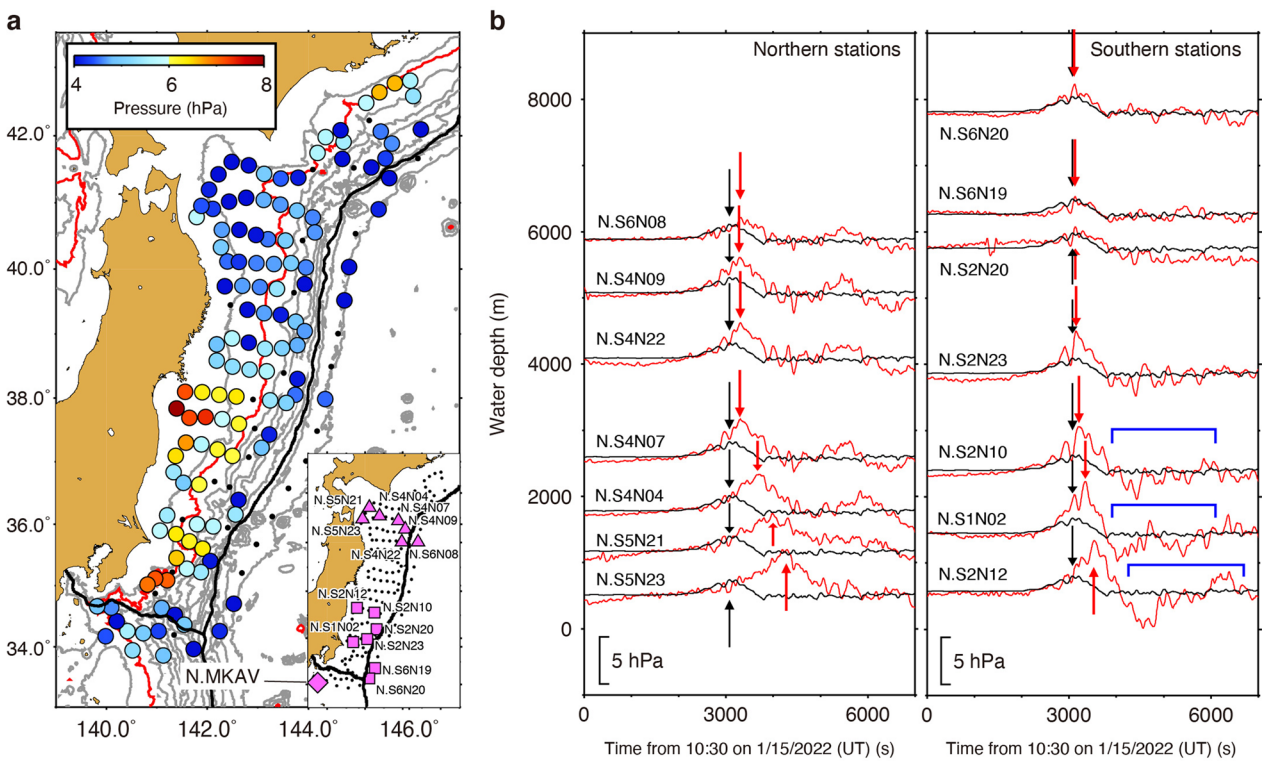

Fig. 3 Amplitudes and waveforms of meteotsunamis and free waves. **a** Peak amplitudes of the first arrivals at each station of S-net. Inset represents the locations of stations used in **b**. **b** (left) Red lines show the time-shifted APG records observed at stations indicated by triangles in the inset in **a**. The black line represents the barometer record observed at N.MKAV in the inset in **a**. Black and red arrows point to the maximum amplitudes of barometer and APG records, respectively. (right) Same as the left panel, but for stations indicated by squares in the inset in **a**. Blue square brackets indicate large amplitudes after the first arrivals

the still water depth. The meteotsunamis and induced free waves are apparently separated by their propagation velocities, because the propagation velocities of meteotsunamis and free waves corresponds to those of the Lamb wave and $\sqrt{gH}$, respectively. The velocity–depth plots that scatter around a constant propagation speed of 0.3 km/s represent the meteotsunami, while those around the $\sqrt{gH}$ curve correspond to the generated free waves. In Fig. 2b, the meteotsunamis are not observed at water depths shallower than 2000 m, suggesting that the maximum amplitudes for the seafloor pressure have been practically converted to free waves at such shallow depths. In many of the northeastern triads, the obtained propagation velocities are faster than those of the long wave (Fig. 2a and Additional file 1: Fig. S2c), which corresponds to the plots around 0.3 km/s at water depths < 4000 m (Fig. 2b).

Although the similar results of the propagation velocity and direction are obtained in the case of the 282 triads, the estimated velocities scatter more widely between 0.3 km/s and the $\sqrt{gH}$ curve, and the estimated directions at some triads are unstable (Additional file 1: Fig. S5). This is because the differential arrival times of the peaks cannot be accurately measured with the small apertures of the triads. In the results from Yamada et al. (2022), velocity–depth plots at water depths of > 3000 m are not matched with both 0.31 km/s and the $\sqrt{gH}$ curve. This may be caused by the use of the small apertures of 225 triads.

Spatial distribution of the amplitudes for first arrivals

Peak amplitudes of the first arrivals rapidly increase as they proceed from the trench to shore in the southern part of the S-net, whereas such a tendency is not clearly observed in the northern part (Fig. 3a). The observed seafloor pressure changes at the northern stations are within a 4–6 hPa range (40.8–61.2 mmH_2O), while the maximum value in the southern stations is approximately 8 hPa (81.6 mmH_2O) nearshore (Fig. 3a and Additional file 1: Fig. S2d). Because the fitted polynomial function, prior to the first arrival, reproduced the observed long period components (Additional file 1: Fig. S1), these

pressure changes and the difference between the northern and southern stations are reliable. Thus, meteotsunamis impinging on the Japan Trench behave differently afterward, depending on whether their incidence is in the northern or southern part. The different behaviors include the propagation velocity (Figs. 1a and 2a) and the amplitude (Fig. 3a) of the peak.

Figure 3b shows the waveforms of the first arrivals in comparison with the barogram from the station (N.MKAV) in the V-net on the Miyakejima Island (Fig. 3a). APG records are appropriately time-shifted for this comparison. The first arrivals of the meteotsunamis and Lamb waves have positive amplitudes at the deep water areas, indicating that the meteotsunamis in the ocean are excited by the Lamb wave propagating with a velocity of 0.29 km/s, which is faster than the $\sqrt{gH}$ value (Garrett 1970).

As shown in Fig. 3b, at water depths > 2000 m, the timings of the peaks and peak-containing pulse durations for the first arrivals recorded in the northern and southern APGs are almost coincident with those recorded by the barometer. However, peaks in the APGs at water depths < 2000 m are gradually delayed from the peak in the barometer record (red arrows in Fig. 3b). Because peaks in the APGs are delayed with decreasing water depth, durations of the pulses become longer at shallower water depths (a peak in the time-shifted APG delayed from that in the barometer record is a delayed peak). Amplitudes of the delayed peaks are larger than those of the peaks at deeper water depths. These observations indicate that the peaks at deeper depths correspond to the meteotsunamis with a propagation velocity of 0.3 km/s and that the delayed peaks correspond to the induced free tsunamis with a speed following the $\sqrt{gH}$ curve as in Fig. 2b. Figures 3b and 2b provide information about how free tsunamis are generated from the meteotsunamis.

Discussion

Free waves generated from the meteotsunamis

We interpret the delayed peaks observed at shallow water depths as free waves generated after the meteotsunamis propagation for the following reason. When a forced wave impinges on a bathymetric step, in addition to the transmitted forced wave, a transmitted free wave is generated in the shallow water depth behind the step (Garrett 1970). Theoretically, for a given form of the meteotsunamis, the amplitude ratio of the transmitted free wave to the transmitted forced wave increases with decreasing water depth (Garrett 1970). Accordingly, the transmitted free waves are generated successively during the Lamb wave propagation at the bathymetric slope, and the forced waves left behind the Lamb waves are apparently replaced by free waves in the bathymetric slope area. This process qualitatively explains the generation of the delayed peak. Tanioka et al. (2022) demonstrated these generations using numerical simulations.

Apparent velocities of the meteotsunamis and generated free waves can be distinguished from 0.3 km/s and the $\sqrt{gH}$ curve. However, some of the obtained velocities of these waves are slightly deviated from their theoretical velocities (Fig. 2b). Because the arrival-time-based estimation of the propagation velocity and direction is robust (Additional file 1: Fig. S3), it appears that deviations are not caused by errors from the grid search estimation, but by the wavefront curvature due to spatial variations of the propagation velocity within a triad. Because we assume the entering of a planar wave to a triad, if differential arrival times at the three stations are deviated from those of the planar wave due to the wavefront curvature, obtained results are slightly different from those for the planar wave. Although apparent velocities cannot be discerned at water depths > 5000 m, two patterns, corresponding to 0.3 km/s and the $\sqrt{gH}$ curve, can be observed at shallower water depths.

The amplitudes of the generated free waves become large via shoaling effects with the relationship between gradients of the bathymetric slope and the propagation directions of the meteotsunamis and generated free waves. Additional file 1: Fig. S2e shows the dip angles for the bathymetry along the propagation direction at the 102 triads. In region (3), the dip angles for the bathymetry along the propagation direction are large (> 4°), and the propagation directions are normal to the dip direction of the bathymetry, where amplitudes of the free waves are developed effectively by decreasing the propagation velocity to preserve energy flux. Narrowing the contour interval of the arrival time at water depths < 2000 m in the southern part (Fig. 1a) is also indicative of the further amplification of the large amplitude via the shoaling effect. In region (2), the propagation direction is oblique to the dip direction of bathymetry, and the energy flux is not efficiently compensated. In region (1), although the dip angles for bathymetry is moderate (2°–3°), the deep water areas extend from the trench, compared to the region at latitudes of 35° N–40° N, and the amplitudes of the forced waves are still preserved (Fig. 2a). Similar features to those in regions (1–2), including the deep water areas from the trench and oblique incidence to the dip direction for bathymetry, are observed in the region (4), and the shoaling effect does not occur effectively. Our results, therefore, indicate that the observed amplitude variations (Fig. 3a) reflect the peaks of the meteotsunamis

in deep water areas near the Japan Trench and those of the generated free waves in the region approaching to nearshore. This implies that, if meteotsunamis come from other directions to the bathymetric slope around the Japan Trench due to future volcanic eruptions, different spatial patterns of the amplification would be observed.

Waveform variation of the meteotsunamis and free waves

Another specific feature from our observations is the long-period negative amplitudes after the first arrivals. Large amplitudes with a negative polarity are gradually evolved when the generated free waves propagate at the bathymetric slope in the southern part of the S-net (blue square brackets in Fig. 3b); however, such negative amplitudes are not observed in the northern part. The dominant period of this negative amplitude is similar to that of the preceding positive peaks. It appears that this negative amplitude is produced through the excitation of free waves generated from meteotsunamis during propagation at the bathymetric slope (Garrett 1970). Tanioka et al. (2022) numerically reproduced negative amplitudes at the bathymetric slope areas. However, to reproduce the spatial variation of the presence and absence of these amplitudes, more detailed simulations, including realistic seafloor bathymetry and coupling mechanisms between the atmosphere and ocean, are required (Vilibić et al. 2016).

Conclusions

We investigated records of a dense observation of the ocean wavefield associated with the 2022 Hunga–Tonga volcanic eruption, focusing on the upslope region of the Japan Trench. We provided the spatial variation of the propagation velocity and direction of the meteotsunamis and the generated free waves in the bathymetric slope areas. Our results show that free waves are generated when the meteotsunamis propagate at the upsloping bathymetry, and sea level changes observed at the coast of Japan are not primarily caused by the meteotsunami itself, but by the free waves progressively generated from them. Particularly, we found a distinct amplitude difference between the northern and southern parts of the S-net. This implies that for future volcanic eruptions, the amplitude distribution of free waves generated from meteotsunamis at the bathymetric slope areas vary with the relationship between the gradient of the bathymetric slope and incoming direction of the Lamb waves.

Abbreviations

S-net: Seafloor Observation Network for Earthquakes and Tsunamis; V-net: Volcano observations network.

Supplementary Information

The online version contains supplementary material available at https://doi.org/10.1186/s40623-022-01727-x.

Additional file 1: Figure S1. Waveform examples for the removal of long-period components. **Figure S2**. Estimated parameters of the meteotsunamis and free waves. **Figure S3**. Geometry for measuring the propagation velocity and direction within a triad. **Figure S4**. Estimation of propagation velocity and direction for a triad. **Figure S5**. Propagation velocity and direction for 282 triads. **Figure S6**. Propagation velocity and direction of the Lamb wave estimated by triads of V-net. **Table S1**. Estimated propagation velocity and azimuth of forced and free waves.

Acknowledgements

We used the absolute pressure gauge data of the Seafloor Observation Network for Earthquakes and Tsunamis (S-net: https://doi.org/10.17598/nied.0007), and the barometer data of the volcano observation network (V-net: https://doi.org/10.17598/nied.0006), operated by National Research Institute for Earth Science and Disaster Resilience. Comments from the editor and two anonymous reviewers greatly improved the manuscript.

Author contributions

TT processed the data, and drafted the manuscript. TT and YF contributed to the interpretation. Both authors read and approved the final manuscript.

Funding

Not applicable.

Availability of data and materials

S-net and V-net data can be downloaded from Monitoring of Waves on Land and Seafloor (MOWLAS) webpage (https://www.mowlas.bosai.go.jp/mowlas/?LANG=en) of National Research Institute for Earth Science and Disaster Resilience.

Declarations

Ethics approval and consent to participate

Not applicable.

Consent for publication

Not applicable.

Competing interests

The authors declare no competing interests.

Received: 21 July 2022 Accepted: 19 October 2022
Published online: 01 November 2022

References

Aoi S, Asano Y, Kunugi T, Kimura T, Uehira K, Takahashi N, Ueda H, Shiomi K, Matsumoto T, Fujiwara H (2020) MOWLAS: NIED observation network for earthquake, tsunami and volcano. Earth Planet Space 72:126

Chen Y, Niu X (2018) Forced wave induced by an atmospheric pressure disturbance moving towards shore. Cont Shelf Res 160:1–9

Defant A (1961) Physical oceanography. Pergamon Press, Oxford

Garrett JR (1970) A theory of the Krakatoa tide gauge disturbances. Tellus 22:43–52

Harkrider D, Press F (1967) The Krakatoa air-sea waves: an example of pulse propagation in coupled systems. Geophys J Int 13:149–159

Kubo H, Kubota T, Suzuki W, Aoi S, Sandanbara O, Chikasada N, Ueda H (2022) Ocean-wave phenomenon around Japan due to the 2022 Tonga eruption observed by the wide and dense ocean-bottom pressure gauge networks. Earth Planets Space 74:104. https://doi.org/10.1186/s40623-022-01663-w

Kubota T, Saito T, Chikasada NY, Sandanbata O (2021) Meteotsunami observed by the deep-ocean seafloor pressure gauge network off Northeastern Japan. Geophys Res Lett 48:e2021GL094255
Kubota T, Saito T, Nishida K (2022) Global fast-traveling tsunamis driven by atmospheric Lamb waves on the 2022 Tonga eruption. Science. https://doi.org/10.1126/science.abo4364
Lamb H (1932) Hydrodynamics. Cambridge University Press, Cambridge
Monserrat S, Vilibić I, Rabinovich AB (2006) Meteotsunamis: atmospherically induced destructive ocean waves in the tsunami frequency band. Nat Hazards Earth Syst Sci 6:1035–1051
Nishida K, Kobayashi N, Fukao Y (2014) Background Lamb waves in the Earth's atmosphere. Geophys J Int 196:312–316
Okuwaki R, Fan W, Yamada M, Osawa H, Wright TJ (2021) Identifying landslides from continuous seismic surface waves: a case study of multiple small-scale landslides triggered by Typhoon Talas, 2011. Geophys J Int 226:729–741
Saito T, Kubota T, Chikasada NY, Tanaka Y, Sandanbata O (2021) Meteorological Tsunami generation due to sea-surface pressure change: three-dimensional theory and synthetics of ocean-bottom pressure change. J Geophys Res Oceans 126(5):e2020JC017011. https://doi.org/10.1029/2020JC017011
Sekizawa S, Kohyama T (2022) Meteotsunami observed in Japan following the Hunga Tonga eruption in 2022 investigated using a one-dimensional shallow-water model. SOLA 18:129–134. https://doi.org/10.2151/sola.2022-021
Tanioka Y, Yamanaka Y, Nakagaki T (2022) Characteristics of the deep sea tsunami excited offshore Japan due to the air wave from the 2022 Tonga eruption. Earth Planets Space 74:61
Umino N, Okada T, Hasegawa A (2002) Foreshock and aftershock sequence of the 1998 M 5.0 Sendai, northeastern Japan, earthquake and its implications for earthquake nucleation. Bull Seis Soc Am 92(6):2465–2477
Vilibić I (2008) Numerical simulations of the Proudman resonance. Cont Shelf Res 28:574–581
Vilibić I, Šepić J, Rabinovich AB, Monserrat S (2016) Modern approaches in meteotsunami research and early warning. Front Mar Sci 3:57. https://doi.org/10.3389/fmars.2016.00057
Wang Y, Satake K (2021) Real-time tsunami data assimilation of S-Net Pressure Gauge Records during the 2016 Fukushima Earthquake. Seis Res Lett 92:2145–2155
Yamada M, Ho T, Mori J, Nishikawa Y, Yamamoto M (2022) Tsunami triggered by the Lamb wave from the 2022 Tonga volcanic eruption and transition in the offshore Japan region. Geophys Res Lett 49:e2022GL098752

Publisher's Note